Absolute parametric decay instabilities of X2 microwave beams in reduced models and fully kinetic codes

Senstius, M. G.; Gusakov, E. Z.; Popov, A. Yu; Nielsen, S. K.

Published in:
Plasma Physics and Controlled Fusion

Link to article, DOI:
10.1088/1361-6587/ac8f6e

Publication date:
2022

Document Version
Peer reviewed version

Absolute parametric decay instabilities of X2 microwave beams in reduced models and fully kinetic codes

M. G. Senstius[1], E. Z. Gusakov[2], A. Yu. Popov[2], S. K. Nielsen[1]

[1]Department of Physics, Technical University of Denmark, Fysikvej, DK-2800 Kgs. Lyngby, Denmark

[2]Ioffe Institute, 26 Polytekhnicheskaya st., St.-Petersburg 194021, Russia

Abstract. Nonlinear wave interactions known as parametric decay instabilities (PDIs) have been known to occur in fusion plasmas for many years. In the past, they have generally been considered of little importance in the context of high power microwave beams aimed for X2 heating due to high thresholds. Experimental evidence suggests that non-monotonic density structures such as islands and ELMs can lead to low thresholds absolute PDIs. The consequences include degraded ECRH performance, absorption into unintended modes and the production of strong scattering which may damage microwave sensitive equipment. We present a reduced analytical 1D model for absolute PDI of an X-mode microwave beam into a cascade of electrostatic eigenmodes of a non-monotonic density structure. The model is solved numerically and compared with fully kinetic particle-in-cell (PIC) simulations which are computationally much more expensive. The primary decay, which initiates cascade, shows good agreement with the PIC simulations in terms of daughter frequencies, growth rates and saturation, in particular in a weakly nonlinear pump intensity regime. The secondary daughter waves of the reduced model, while visible, do not appear to be the dominant processes in the PIC simulations.

1. Introduction

A myriad of electromagnetic as well as electrostatic waves are able to propagate in a magnetized plasma. Modes with various properties exist which allow them to be utilized to diagnose and manipulate both laboratory plasmas but also naturally occurring plasmas such as in the ionosphere. Being a nonlinear medium, a plasma may furthermore facilitate a type of nonlinear wave interactions sometimes referred to as parametric instabilities[1, 2, 3, 4, 5, 6, 7, 8, 9, 10, 11]. The most common example is of a pump wave which can become unstable to decay into a number of lower frequency daughter waves if energy and momentum are conserved in the process, and if the pump wave amplitude exceeds a threshold. This process is known as a parametric decay instability (PDI) and can be further characterized as an absolute or convective PDI depending on whether the daughter waves grow exponentially in time or experience limited spatial amplificaiton as they are convected through the decay region. The pump wave amplitude threshold varies greatly depending on local plasma parameters and their profiles. In fusion plasmas, PDIs have generally been considered best avoided when injecting high power microwaves into the plasma for electron cyclotron (EC) resonance heating (ECRH), current drive (ECCD) and diagnostics. This is because PDIs would drain the power of the injected beam while producing daughter waves, which currently have little use. The result would be that energy is absorbed into unintended regions of the plasmas leading to degraded ECRH and ECCD while producing daughter waves that could damage microwave sensitive equipment[15].

In magnetized fusion plasmas, ECRH and ECCD at low harmonics of the EC resonance are popular due to good accessibility to most regions of the plasma and efficient high power sources such as gyrotrons[16, 17]. The first observations of PDIs during ECRH experiments were made in the Versator II tokamak[18]. An optically thin fundamental EC resonance meant that the injected beam was only partially absorbed and a significant amount of power was able to reach the upper hybrid (UH) layer. At the UH layer, X-mode waves are more likely to suffer from convective PDIs due to wave amplification[19]. The PDIs produced waves shifted by characteristic ion frequencies which were measured outside the plasma. Similar observations were later made in the Wendelstein 7-A stellarator[20] and more recently in the ASDEX Upgrade tokamak[21]. Although PDIs currently find no applications in magnetically confined fusion, there have been reports of high energy ions in ECRH experiments[22, 23, 24] which may be explained by such PDIs. In higher density plasmas of contemporary devices like the ASDEX Upgrade tokamak and the Wendelstein 7-X stellarator, the fundamental EC resonance is typically not accessible. When aiming a beam for higher EC harmonics, the UH layer is not reached and PDIs have therefore mostly been considered of little importance at current ECRH and ECCD power levels. However, observations of scattering during second harmonic ECRH in the TEXTOR tokamak[25, 26] resembling that from PDIs at the UH layer suggested that a previously not thought of mechanism was reducing the PDI threshold significantly. Theoretical models[27, 14, 28] argue that

the presence of a non-monotonic density structure near the second harmonic UH layer can give rise to absolute PDIs involving UH waves trapped in the structure. In the case of the TEXTOR experiments, the non-monotonic structure was a magnetic island. Similar observations have since been made in ASDEX Upgrade[15] and Wendelstein 7-X[29]. Power absorption caused by PDIs into trapped waves in the non-monotonic structures is very sensitive to the plasma parameters of the structures. Experiments at the linear device GRANIT[30] have shown 45% steady absorption of injected waves. Such a rate of absorption in a fusion reactor would have a devastating effect on the ECRH and ECCD performance.

Ideally, a model describing PDIs into trapped UH waves should be fully kinetic. However, it is difficult to make much progress analytically without having to impose a number of assumptions which neglect certain plasma effects or limit the number and characteristics of the interacting waves. Provided that the assumptions are appropriate, a reduced model that captures the essence of the problem can be obtained. An alternative approach is to use high performance computing to conduct a fully kinetic investigation numerically with minimal assumptions about the behavior of the plasma. However, this approach is often computationally exceedingly expensive. In practice, fully kinetic simulations usually require simplifications to the geometry such as a reduction in the dimensionality of the problem and cannot be run on an average computer to aid ECRH and ECCD beam planning with short notice. A reduced model that captures the essentials of the problem can speed up predictions substantially. In this paper, we investigate how a reduced model of PDIs in non-monotonic density structures[14, 28, 31, 32] compare to fully kinetic particle-in-cell (PIC) simulations[33, 34] of the same problem. As a starting point, a simplified 1D geometry is used for both the the PIC simulations and the reduced model. The two approaches have rather different assumptions and should therefore not suffer from the same limitations. The 1D simplification means that this investigation is not comparable with any particular tokamak or stellarator experiments. Still, the comparison in 1D allows for some key features of the reduced models to be checked in a setting where the PIC simulation data analysis is much clearer. It is found that a low pump intensity regime exists where the low threshold absolute PDI is dominant and both models agree well on the primary decay process which initiates a cascade of decays. The reduced models can therefore be expected to predict thresholds for absolute PDIs well. The secondary decays, which saturate the primary decay, are found to differ between the two models.

2. Theory

2.1. PDI theory

The three-wave interaction is perhaps the simplest and most common type of nonlinear phenomena in plasmas. It becomes resonant if the following selection rules for frequency

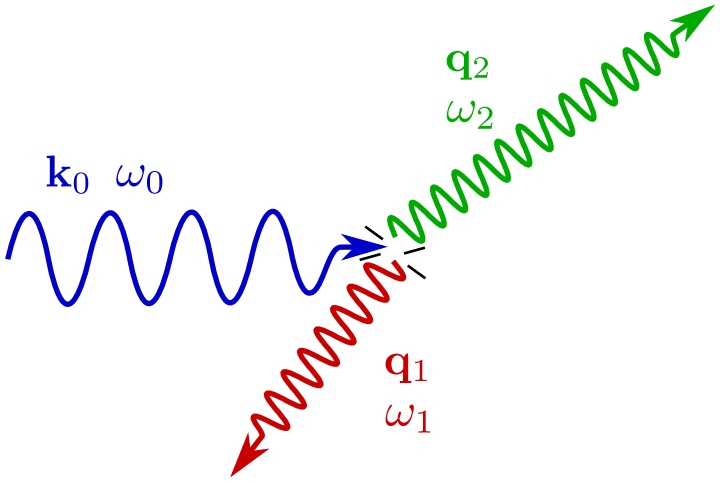

Figure 1. Illustration of a three-wave decay event in which a strong pump $(\mathbf{k}_0, \omega_0)$ excites two daughter waves $(\mathbf{k}_1, \omega_1)$ and $(\mathbf{k}_2, \omega_2)$. The decay must satisfy the ω- and $\mathbf{k}$-selection rules in equation (1), conserving both energy and momentum locally.

and wave number are satisfied

$$\begin{aligned} \omega_0 &= \omega_1 + \omega_2 \\ \mathbf{k}_0 &= \mathbf{q}_1 + \mathbf{q}_2, \end{aligned} \tag{1}$$

where ω_i is the angular frequency of the i^{th} interacting wave, $\mathbf{k}_0$ is the wave number of wave 0, and $\mathbf{q}_1$ and $\mathbf{q}_2$ are the wave numbers of the other two waves. The above form is typically associated with the decay of wave 0, referred to as the pump wave, into the waves 1 and 2, referred to as daughter waves, as illustrated in figure 1. If this three-wave interaction becomes unstable, it is commonly referred to as a PDI. In a homogeneous plasma, the pump wave amplitude threshold for the instability is determined by collisional or resonant absorption of the interacting waves[1, 2, 3, 4, 5, 6, 7, 8]. This instability is absolute and the daughter waves grow exponentially in time above the threshold until either the pump wave depletion occurs or other nonlinear effects saturate the process.

In an inhomogeneous plasma, the selection rules may only be satisfied locally and convection of daughter waves through this region can strongly affect the nonlinear coupling and even stabilize the PDI. An interaction region of length l_d may exist in which the selection rules are approximately satisfied. The length of this region is typically estimated from the waves numbers as $l_\mathrm{d} \approx |\partial \Delta K(x)/\partial x|_{x_\mathrm{d}}^{-1/2}$ in 1D, where $\Delta K(x) \equiv k_0(x) - q_1(x) - q_2(x)$ is the wave number mismatch and x_d is the exact point where the decay conditions are satisfied. The instability can temporarily become absolute inside this region when following the daughter waves if the threshold for the homogeneous PDI is exceeded. On the whole, the daughter waves will have seen a finite amplification when the interaction region has been traversed. However, this amplification may not be significant if the decay region is short, if the nonlinear coupling of the waves is weak or if waves are heavily damped. The notion of a threshold therefore also changes in an inhomogeneous plasma; an instability can occur locally with no

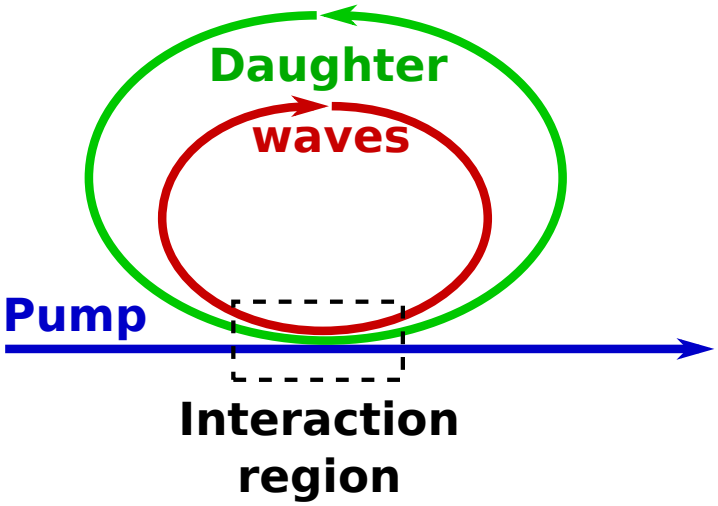

Figure 2. Simple illustration of an absolute PDI where a pump wave excites two daughter waves through PDI inside a finite interaction region. Because the daughter waves are able to return to the interaction region, the waves continue to interact and the instability therefore becomes absolute in time.

noticeable impact. The instability threshold for the so called convective PDI is often given through the coefficient of spatial amplification[9, 10, 11, 13]

$$Z = \frac{|\nu_0|^2 \, l_d^2}{|u_1| \, |u_2|}, \tag{2}$$

where ν_0 is the growth rate of the daughter waves in a homogeneous plasma, and u_1 and u_2 are the group velocities of the daughter waves. Although threshold values of Z are often a matter of convention, the case of $Z \ll 1$ is a situation where the nonlinear coupling is too weak for the convective PDI while $Z > 1$ may lead to a substantial amplification of the daughter waves. The properties of the convective PDI in inhomogeneous plasmas were reviewed in [6, 35].

Under the right circumstances, an absolute PDI may also occur in inhomogeneous plasmas. The absolute PDI is possible if the daughter waves are able to return to the interaction region, see figure 2. The mechanisms that localize the daughter waves in the vicinity of the interaction region may vary but the impact on the plasma can be substantial even for $Z \ll 1$, provided the amplification in the interaction region exceeds the daughter wave losses in a round trip. The result is that the daughter waves may experience an exponential growth in time[36, 37] even for weak nonlinear coupling. The growth is eventually saturated either because of pump wave depletion or because of other nonlinear effects which set in when the amplitudes of the daughter waves have increased sufficiently. In non-monotonic density profiles, UH waves can become trapped if multiple UH layers exist. In this case, the density profile acts as a cavity with characteristic UH eigenmodes which has been studied using the WKB approximation to produce reduced models of coupled equations[14, 28, 32] but also using PIC simulations[33, 34]. These approaches will be compared here.

2.2. Wave descriptions

In this investigation, the pump wave is a fast X-mode wave and the PDI daughter waves are UH waves. In order to reduce the complexity of the comparison, the plasma as well as the electric and magnetic fields are assumed to be homogeneous in all but one dimension. The inhomogeneous direction is denoted by x and the magnetic field is chosen to be perpendicular to this direction. To conform with the 1D PIC simulations presented later in this paper, all waves are assumed to only propagate in the x-direction and the background magnetic field is entirely uniform. Although the waves propagate primarily perpendicularly to the magnetic field in physical plasmas, the assumption of only one inhomogeneous direction means that this investigation is not directly comparable to experiments where losses due to dynamics in the direction parallel to can be important for PDI thresholds and interaction rates. With these assumptions, the wave number of the fast X-mode pump wave takes the form

$$k_{0x}(x) = \frac{\omega_0}{c}\sqrt{\frac{S(\omega_0,x)^2 - D(\omega_0,x)^2}{S(\omega_0,x)}}, \tag{3}$$

with the Stix parameters defined as $S(\omega,x) \equiv 1 - \omega_{\mathrm{pe}}(x)^2/(\omega^2 - \omega_{\mathrm{ce}}^2)$ and $D(\omega,x) \equiv \omega_{\mathrm{ce}}(x)\omega_{\mathrm{pe}}^2/[\omega(\omega^2 - \omega_{\mathrm{ce}}^2)]$, where $\omega_{\mathrm{pe}}(x) \equiv \sqrt{e^2 n_{\mathrm{e}}(x)/(\epsilon_0 m_{\mathrm{e}})}$ is the electron plasma angular frequency, $\omega_{\mathrm{ce}} \equiv eB/m_{\mathrm{e}}$ is the electron cyclotron angular frequency, $n_{\mathrm{e}}(x)$ is the electron density, B is the background magnetic field amplitude, m_{e} is the electron mass, e is the elementary charge, c is the vacuum speed of light and ϵ_0 is the vacuum permittivity. Note that ω_{ce} is defined using the elementary charge, e, and not the electron charge, $-e$.

The primary PDI daughter waves are assumed to be a pair of UH waves satisfying the dispersion relation[38]

$$\mathcal{D}_{\mathrm{UH}}(q_x,\omega) = q_x^2 + \frac{2\omega_{\mathrm{pe}}^2}{v_{\mathrm{Te}}^2}\left[1 - \sum_{j=-\infty}^{\infty}\frac{\omega}{\omega - j\omega_{\mathrm{ce}}}\exp\left(-\frac{q_x^2 v_{\mathrm{Te}}^2}{2\omega_{\mathrm{ce}}^2}\right) I_j\left(\frac{q_x^2 v_{\mathrm{Te}}^2}{2\omega_{\mathrm{ce}}^2}\right)\right] + \frac{\omega^2}{c^2}D(\omega,x)^2 = 0 \tag{4}$$

where $v_{\mathrm{Te}}^2 \equiv 2T_{\mathrm{e}}/m_{\mathrm{e}}$ is the electron thermal velocity, with T_{e} being the electron temperature in units of electron volts.

For the secondary decays, one daughter wave is assumed to be an IBW while the other is a correspondingly downshifted UH wave. The dispersion relation for the IBWs is[38]

$$\mathcal{D}_{\mathrm{IB}}(q_x,\omega) \equiv q_x^2 + \sum_{\sigma=\mathrm{e,i}}\frac{2\omega_{\mathrm{p}\sigma}^2}{v_{\mathrm{T}\sigma}^2}\left[1 - \sum_{j=-\infty}^{\infty}\frac{\omega}{\omega - j\omega_{\mathrm{c}\sigma}}\exp\left(-\frac{q_x^2 v_{\mathrm{T}\sigma}^2}{2\omega_{\mathrm{c}\sigma}^2}\right) I_j\left(\frac{q_x^2 v_{\mathrm{T}\sigma}^2}{2\omega_{\mathrm{c}\sigma}^2}\right)\right] = 0, \tag{5}$$

where the sum of σ corresponds to electron and ion contributions. Both dispersion relations in equations (4) and (5) are solved numerically.

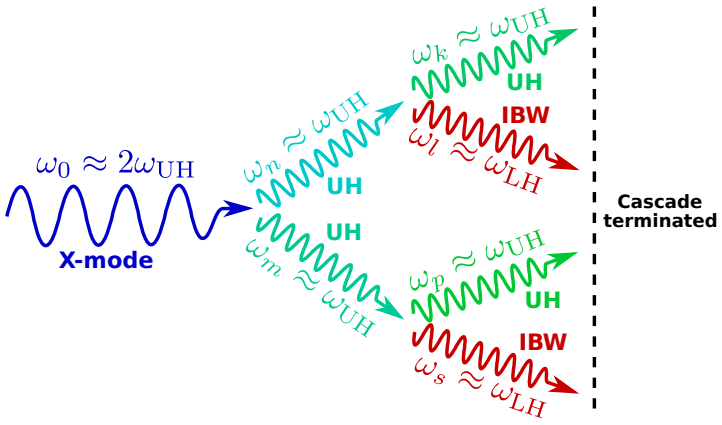

Figure 3. An illustration of the decay cascade considered in the reduced model. The cascade is initiated by a free X-mode wave near the second harmonic UH layer. This pump wave excites two trapped UH waves which in turn each excite one UH and one IBW. The frequency labels and ranges as well as types of waves are indicated at each wave.

2.3. Decay cascade

Neither UH waves nor IBWs propagate in vaccuum. As they propagate to lower density, they eventually reach low density reflection points. Both types of waves can therefore be trapped and form eigenmodes in appropriate non-monotonic density profiles. In the WKB approximation, the eigenmodes obtain an integer multiple of 2π phase difference when they perform a roundtrip through the trapping region. The wave encounters two turning points during the roundtrip and the wave gets a phase shift of $\pi/2$ at each of these points[39]. The eigenmodes therefore satisfy the quantization condition

$$\int_{x_\mathrm{l}}^{x_\mathrm{r}} |q_x^+| - |q_x^-| \mathrm{d}x = \pi\,(2p+1)\,, \quad p \in \mathbb{Z}, \tag{6}$$

where q_x^+ and q_x^- are the hot and cold wave numbers of an eigenmode in the direction of the inhomogeneity, and x_l and x_r are the left and right turning points of the mode. In the present article, an X-mode pump wave initiates a cascade of decays into eigenmodes of a non-monotonic density profile as the pump wave propagates through it. It is assumed that a single primary decay from the pump wave into two approximately half frequency UH eigenmodes dominates and no other primary process has any significance. Quantities with the subscripts n and m refer to the primary daughter waves.

Each of the primary daughter waves are assumed to further decay in a single secondary process, exciting an IBW eigenmode of much lower frequency as well as a correspondingly downshifted UH eigenmode. The primary daughter wave n excites the IBW l and the UH wave k, while the other primary daughter wave m correspondingly excites s and p. The cascade continues until cumulative losses prevent further decay from becoming unstable. However after the secondary decays, the cascade in the present reduced model is terminated but could in principle be continued to achieve a more accurate model. The cascade is illustrated in figure 3.

To describe the dynamics of the cascade of PDIs, the daughter waves are all assumed to be electrostatic and Poisson's equation is split into contributions associated with each of the daughter waves

$$\nabla^2\varphi_j(\mathbf{r},t) = -\frac{\rho_{j,l}(\mathbf{r},t)+\rho_{j,nl}(\mathbf{r},t)}{\varepsilon_0}, \tag{7}$$

where φ_j is the electrostatic potential and $\rho_{j,l}, \rho_{j,nl}$ are the linear and nonlinear charge densities associated with the jth wave. Through the charge conservation equation and the convolution theorem, the linear charge density can be described using the linear dispersion relation for the wave[14, 32, 40]

$$\int_{\text{all }(\mathbf{r}',t')} \frac{1}{(2\pi)^4} \int_{\text{all }(\mathbf{q},\omega)} \mathcal{D}(\mathbf{q},\omega)\exp\left(i\mathbf{q}\cdot[\mathbf{r}-\mathbf{r}'] - i\omega[t-t']\right)\,\mathrm{d}\mathbf{q}\mathrm{d}\omega\,\varphi_j(\mathbf{r}',t')\,\mathrm{d}\mathbf{r}'\mathrm{d}t' = \frac{\rho_{j,nl}(\mathbf{r},t)}{\varepsilon_0}.$$

The nonlinear charge density can be described using the nonlinear susceptibilities of the plasma, $\chi_e^{(a,b)}$, as in [32] and the amplitude of the other waves interacting with it. For the primary daughter wave m, the nonlinear charge density is

$$\frac{\rho_{m,nl}(\mathbf{r},t)}{\varepsilon_0} = -\frac{\left(\chi_{\mathrm{e}}^{(a)}(\mathbf{r},t)\right)^* E_0^*(\mathbf{r},t)\varphi_n(\mathbf{r},t)}{2B} - \frac{e}{T_e}\chi_{\mathrm{e}}^{(b)}(\mathbf{r},t)\varphi_p^*(\mathbf{r},t)\varphi_s(\mathbf{r},t), \tag{9}$$

where superscript $*$ means complex conjugation and the pump wave electric field is given by

$$E_0(\mathbf{r},t) = \frac{1}{2}\sqrt{\frac{8\pi I_0}{c}}\sqrt{\frac{\omega_0}{ck_{0x}(x)}}\exp\left(i\int^x k_{0x}(x')\mathrm{d}x' - i\omega_0 t\right), \tag{10}$$

defined through its intensity I_0. The nonlinear susceptibilities are given by[32]

$$\chi_{\mathrm{e}}^{(a)} = -\frac{\omega_{\mathrm{pe}}^2\omega_{\mathrm{ce}}^2\omega_0^2}{(\omega_0^2-\omega_{\mathrm{ce}}^2)(\omega^2-\omega_{\mathrm{ce}}^2)^2}\frac{q_{m\mathrm{x}}q_{n\mathrm{x}}k_{0x}c}{4\omega_0}\left(7+3\frac{D(\omega_0,x)\omega_0}{S(\omega_0,x)\omega_{\mathrm{ce}}}-\frac{4\omega_{\mathrm{ce}}^2}{\omega_0^2}\right) \tag{11}$$

$$\begin{aligned}\chi_{\mathrm{e}}^{(b)} = &-iq_{m\mathrm{x}}q_{p\mathrm{x}}q_{s\mathrm{x}}\frac{\omega_{\mathrm{pe}}^2}{\omega_{\mathrm{ce}}^3}\sum_{p',m'}\int_0^\infty v_\perp f_{\mathrm{M}}\Bigg[\frac{(m'+p')p'}{(p'-\alpha_m)(m'+p'-\alpha_s)}\frac{J_{m'+p'}(\lambda_s)}{\lambda_s}\frac{J_{p'}(\lambda_m)}{\lambda_m}J'_{m'}(\lambda_p)\\ &+\frac{(p'+m')m'}{(m'-\alpha_p)(p'+m'-\alpha_s)}\frac{J_{p'+m'}(\lambda_s)}{\lambda_s}J'_{p'}(\lambda_m)\frac{J_{m'}(\lambda_p)}{\lambda_p}\\ &+\frac{p'm'}{(m'-\alpha_p)(p'-\alpha_m)}J'_{p'+m'}(\lambda_s)\frac{J_{p'}(\lambda_m)}{\lambda_m}\frac{J_{m'}(\lambda_p)}{\lambda_p}\Bigg]\mathrm{d}v_\perp.\end{aligned} \tag{12}$$

Here, subscript 0 refers to the pump wave, m and n refer to primary UH daughter waves, p refers to a secondary UH daughter wave and s to a secondary ion wave. The q_{mx} is the wavenumber, $\lambda_m = q_{m\mathrm{x}}v_\perp/\omega_{\mathrm{ce}}$, $\alpha_m = \omega_m/\omega_{\mathrm{ce}}$ and similar for the other subscripts. The $J_{m'}(\lambda_m)$ and $J'_{m'}(\lambda_m)$ are the Bessel function of the first kind and its derivative. The f_{M} is a Maxwellian distribution function over perpendicular velocities normalized as $\int_0^\infty f_{\mathrm{M}}v_\perp\mathrm{d}v_\perp = 1$. Returning to equation (9), the first term on the right hand side is the nonlinear charge density associated with the primary decay whereas the last term is associated with the secondary decay. The expression is similar for the other modes. It is assumed that the pump wave is not depleted by the cascade of decays. Assuming that the daughter waves are eigenmodes of a non-monotonic density structure, a solution

is sought in terms of a function proportional to the potential of the eigenmode, ϕ_m, a phase and a time dependent amplitude, a_m,

$$\varphi_m(\mathbf{r},t) = a_m(t)\phi_m(x)\exp\left(-i\omega_m t\right). \tag{13}$$

The amplitude is assumed to depend on time on a scale much slower than its inverse frequency, ω_m^{-1}, and it is normalized such that $T_e|a_m|^2$ gives the UH wave energy density averaged over its trapping region. In a 3D geometry of a tokamak or stellarator, an eigenmode in the direction perpendicular to the magnetic field can usually be excited because the wavenumber parallel to the magnetic field is a free parameter, which can modify the frequency of the modes to fit the PDI selection rules. In 1D, the parallel wavenumber is zero, so if the selection rules in equation (1) do not satisfy decay into an exact eigenmode, a superposition eigenmodes are excited with the closest eigenfrequency being the strongest of them. Whilst the primary decay is able to excite UH eigenmodes exactly for the parameters presented later, the secondary decays are not so we seek a solution for the IBW mode s of the form

$$\varphi_s(\mathbf{r},t) = \sum_j b_{s,j}(t)\phi_j(x)\exp\left(-i\omega_j t\right), \tag{14}$$

and similar for the other IBW, l. Because the eigenmodes are being forced with a frequency other than their characteristic eigenfrequency, their amplification is impeded which increases with the frequency mismatch between the forced and characteristic frequencies, $\Delta_s = \omega_m - \omega_p - \omega_j$, as has also been seen numerically in [34]. The mode closest to the forced frequency is denoted by simply b_s in later calculations. Similar assumptions are made for the remaining waves and substituted into equation (8) along with the appropriate dispersion relations. Performing the averaging procedure over the eigenmode trapping region discussed in [14, 32], a system of coupled differential equations describing the full cascade can be obtained. Below, we simply quote the resulting system of equations for this cascade of PDIs

$$\begin{aligned}
&\frac{\partial a_m}{\partial t} + \nu_{em}a_m = \gamma_0^*\frac{\Delta L_{pr}}{L}a_n - \omega_m\zeta_{mps}b_s a_p^*\exp(i\Delta_s t),\\
&\frac{\partial a_p}{\partial t} + \nu_{ep}a_p = \omega_p\zeta_{mps}b_s a_m^*\exp(i\Delta_s t),\\
&\frac{\partial b_s}{\partial t} + \nu_s b_s + \nu(b_s)b_s = \omega_s\zeta_{mps}a_m a_p\exp(-i\Delta_s t),\\
&\frac{\partial a_n}{\partial t} + \nu_{en}a_n = \gamma_0\frac{\Delta L_{pr}}{L}a_m - \omega_n\zeta_{nkl}b_l a_k^*\exp(-i\Delta_l t),\\
&\frac{\partial a_k}{\partial t} + \nu_{ek}a_k = \omega_k\zeta_{nkl}b_l a_n^*\exp(-i\Delta_l t),\\
&\frac{\partial b_l}{\partial t} + \nu_l b_l + \nu(b_l)b_l = \omega_l\zeta_{nkl}a_n a_k\exp(i\Delta_l t),
\end{aligned} \tag{15}$$

where ν_{em} and similar are the collisional damping rates of UH daughter waves, ν_s and similar are the collisional damping rates of the IBWs, $\Delta L_{pr}/L = \int_{-\infty}^{\infty}\exp(i\int_0^x \Delta K dx')dx/\sqrt{L_m L_n}$, $L_{m,n}$ are the lengths of the trapping region of the indicated mode, and $\Delta\omega_{s,l}$ are the frequency difference between the forced PDI daughter

frequency satisfying the selection rules and the closest eigenfrequency. The remaining quantities ζ_{mps}, ζ_{nkl}, γ_0 and ν_b are longer expressions. The interaction coefficient ζ_{mps} is given by[32]

$$\zeta_{mps} = \sqrt{\frac{q_{mx}^2 q_{px}^2 q_{sx}^2}{\omega_m \mathcal{D}^m_{\mathrm{UH},\omega} \omega_p \mathcal{D}^p_{\mathrm{UH},\omega} \omega_s \mathcal{D}^s_{\mathrm{IB},\omega}}} \sqrt{\frac{4\pi I_e}{B^2} \frac{l^2_{\mathrm{d},mps}}{L_m L_p L_s}} \times \frac{\omega_{\mathrm{pe}}^2 \omega_{\mathrm{ce}} \omega_m \omega_p \omega_s}{(\omega_m^2 - \omega_{\mathrm{ce}}^2)(\omega_p^2 - \omega_{\mathrm{ce}}^2)(\omega_s^2 - \omega_{\mathrm{ce}}^2)} \left[\frac{cq_{px}}{\omega_p} - \frac{cq_{mx}}{\omega_m} - \frac{cq_{sx}}{\omega_s} \right] \Bigg|_{x_{mps}}, \quad (16)$$

and similar for ζ_{nkl}. In the expression above, $I_e = T_e/1\,\mathrm{cm}^2$ and $l_{\mathrm{d},mps} = \int_{-\infty}^{\infty} \exp\left(i \int_{-\infty}^{x} \Delta K_{mps}(x') \mathrm{d}x' \right) \mathrm{d}x \approx 2\pi l_{mps} \mathrm{Ai}\left(-\frac{\Delta K_{mps}(x_{mps})}{l_{mps}} \right)$. The $\mathrm{Ai}(x)$ is the Airy function and the simplification of $l_{\mathrm{d},mps}$ is assuming that the wavenumber mismatch, $\Delta K_{mps}(x)$, is nearly parabolic, defining $l_{mps} = \left(\frac{\partial^2 \Delta K_{mps}(x)}{2\partial x^2} \right)^{-1/3} \Big|_{x_{mps}}$ and x_{mps} as a solution to $\frac{\partial \Delta K_{mps}(x_{mps})}{\partial x} = 0$. The quantities $\mathcal{D}^m_{\mathrm{UH},\omega} = \langle | \partial \mathcal{D}_{\mathrm{UH}} / \partial \omega |_{\omega_m, q_{mx}} \rangle$ and $\mathcal{D}^s_{\mathrm{IB},\omega} = \langle | \partial \mathcal{D}_{\mathrm{IB}} / \partial \omega |_{\omega_s, q_{sx}} \rangle$ are the frequency derivatives of the dispersion relation for the mode indicated in the superscript averaged over the trapping region of the mode. The averaging procedure is defined as

$$\langle \mathcal{D}(q_{mx}, \omega_m) \rangle = \int_{x_{\mathrm{l},m}}^{x_{\mathrm{r},m}} \frac{\mathcal{D}(q^+_{mx}, \omega_m)}{|L^+_m|} + \frac{\mathcal{D}(q^-_{mx}, \omega_m)}{|L^-_m|} \mathrm{d}x, \quad (17)$$

where q^+_{mx} is the hot and q^-_{mx} the cold solution to the relevant dispersion relation $\mathcal{D}(q_x, \omega)$, e.g. the EBW and X-mode solution for UH waves, and $x_{\mathrm{l},m}$ and $x_{\mathrm{r},m}$ are the left and right turning point of the mode, i.e. where the cold and hot solutions meet. The $L^\pm_m$ are the geometric-optic lengths of the path between turning points, calculated as

$$L^\pm_m = \frac{\partial \mathcal{D}(q_x, \omega)}{\partial q_x} \Big|_{q^\pm_{mx}, \omega_m} \int_{x_{\mathrm{l},m}}^{x_{\mathrm{r},m}} \left[\frac{\partial \mathcal{D}(q_x, \omega)}{\partial q_x} \Big|_{q^+_{mx}, \omega_m} \right]^{-1} + \left[\frac{\partial \mathcal{D}(q_x, \omega)}{\partial q_x} \Big|_{q^-_{mx}, \omega_m} \right]^{-1} \mathrm{d}x. \quad (18)$$

The homogeneous growth rate γ_0 of the primary decay is

$$\gamma_0 = -i \frac{1}{2\sqrt{\langle D_{m\omega} \rangle \langle D_{n\omega} \rangle} B} \sqrt{\frac{8\pi I_0}{c}} \sqrt{\frac{\omega_0}{c k_{0x}(0)}} \chi_e^{(a)}(0). \quad (19)$$

Lastly, $\nu(b_s)$ is the amplitude dependent damping coefficient for the IBW b_s as described in [41] and it is calculated by

$$\nu(b_s) = \frac{2\omega_{\mathrm{pi}}^2}{v_{\mathrm{Ti}}^2 \langle \mathcal{D}^s_{\mathrm{IB},\omega} \rangle} \frac{\sqrt{\pi}\omega_s}{\langle q_{sx} \rangle v_{\mathrm{Ti}}} \exp\left(-\frac{\omega_s^2}{\langle q_{sx} \rangle^2 v_{\mathrm{Ti}}^2} \right) \left(1 - \left[\frac{b_s^{\mathrm{th}}}{b_s} \right]^2 \right)^2 H(b_s - b_s^{\mathrm{th}}), \quad (20)$$

where $\langle q_{sx} \rangle$ is the wave number averaged over the trapping region performed similarly to equation (17), $H(b)$ is the Heaviside function and b_s^{th} is the threshold for stochastic IBW damping to become significant, which is given by

$$b_s^{\mathrm{th}} = \frac{1}{8} \left(\frac{\omega_{\mathrm{ci}}}{\omega_s} \right)^{1/3} \frac{\omega_s}{\langle q_{sx} \rangle c} \sqrt{\omega_s \frac{\langle \mathcal{D}^s_{IB,\omega} \rangle}{\langle q_{sx} \rangle^2}} \sqrt{\frac{B^2 L_s}{4\pi I_e}}. \quad (21)$$

Similar expressions apply to all other waves in the system of equations (15) by changing the sub- and superscripts appropriately. Note that only the IBW modes closest to the

forced frequencies are included in the system of equations (15) as the rest are assumed to experience negligible coupling to the remaining waves.

Once all the frequencies of the implicated waves have been determined and all the tedious quantities above have been calculated, the system of equations in (15) can be integrated numerically in time rather cheaply.

2.4. Choice of parameters

Plasma parameters are chosen such that an $\omega_0/(2\pi) \equiv f_0 = 140$ GHz pump frequency is just under twice the UH frequency at the center of the domain. We pick a homogeneous background magnetic field of $B = 2.4$ T, a homogeneous temperature with $T_e = T_i = 100$ eV, and a background density profile of $n_e(x) = n_i(x) = n_0 \exp(-[x/\ell]^2)$, where $n_0 = 5.1 \times 10^{19}$ m^{-3}, $\ell = 10$ mm and the ions are protons. Although these parameters can be obtained at present day fusion devices, the geometry does not reflect what is observed in such machines. This setting is a simplified model to compare with 1D PIC simulations shown in section 3.

2.5. Primary decay

For these parameters, the dominant primary decay process is into mode $n = 6$, $\omega_n/(2\pi) = 70.0168$ GHz, and mode $m = 9$, $\omega_m/(2\pi) = 69.9832$ GHz. The trapping regions can be seen in figure 4. The growth rate of this process is predicted by the model to be $\gamma_0 = 1.3 \times 10^{-2}$ ns^{-1} for a pump intensity of $I_0 = 0.003$ kW/mm^2 and $\gamma_0 = 2.4 \times 10^{-1}$ ns^{-1} for a pump intensity of $I_0 = 1$ kW/mm^2. This is the pump intensity range that will be compared to PIC simulations later. The relationship between the growth rate and the pump intensity is $\gamma \sim I_0^{1/2}$ in this range.

2.6. Secondary decay

For the dominant secondary processes, we find the IBWs that maximize the interaction coefficient while satisfying the ω- and k-matching conditions for each of the primary daughter waves acting as the pump. For the primary daughter wave ω_m, the dominant secondary process is found to excite an IBW of $\omega_s/(2\pi) = 0.5615$ GHz and figure 5 shows the k-matching condition. For the other primary daughter wave ω_n, the IBW daughter frequency is $\omega_l/(2\pi) = 0.5604$ GHz, see figure 6. In both cases, the IBW daughter waves has a frequency greater than but close to the lower hybrid frequency which peaks at a value of 0.4542 GHz at the center of the density profile.

2.7. Mode evolution

Integrating the system of equations (15) in time with initial values of $a_{m,p,n,k} = 1$ and $b_{s,l} = 1$, corresponding to their thermal level, figures 7 and 8 are obtained. Each show the evolution of a primary daughter mode as well as that of the daughter modes of its subsequent decay. Both figures exhibit similar behavior with only minor differences

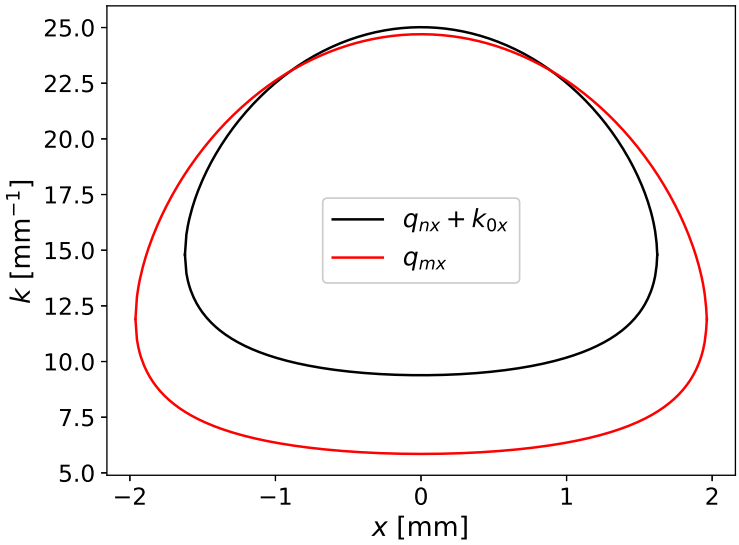

Figure 4. The primary decay process with the highest growth rate is for $\omega_m/(2\pi) = 69.9832$ GHz and $\omega_n/(2\pi) = 70.0168$ GHz. The wavenumbers of the pump wave, k_{0x}, and the daughter waves q_{mx} and q_{nx} in the figure are all positive. Consequently, the daughter waves move in opposite directions as the k-matching condition here is $k_{0x} = -q_{nx} + q_{mx}$.

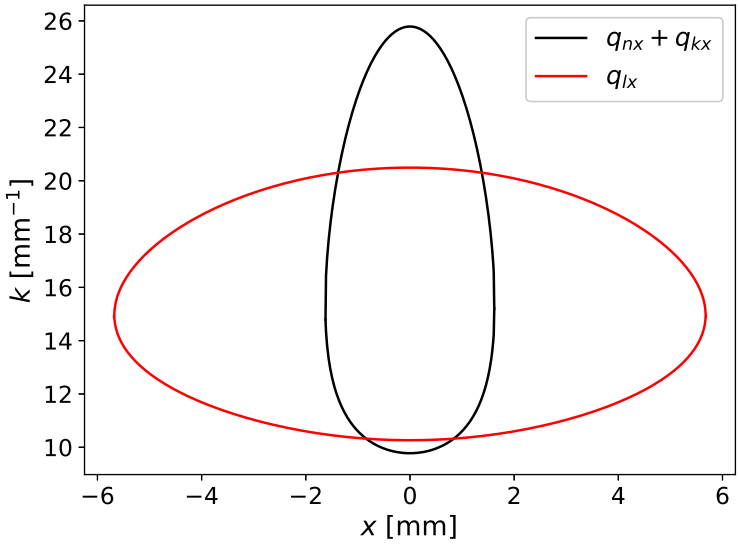

Figure 5. Dominant secondary decay for the primary daughter wave $\omega_n/(2\pi) = 69.9832$ GHz into the IBW $\omega_l/(2\pi) = 0.5604$ GHz and a downshifted UH wave.

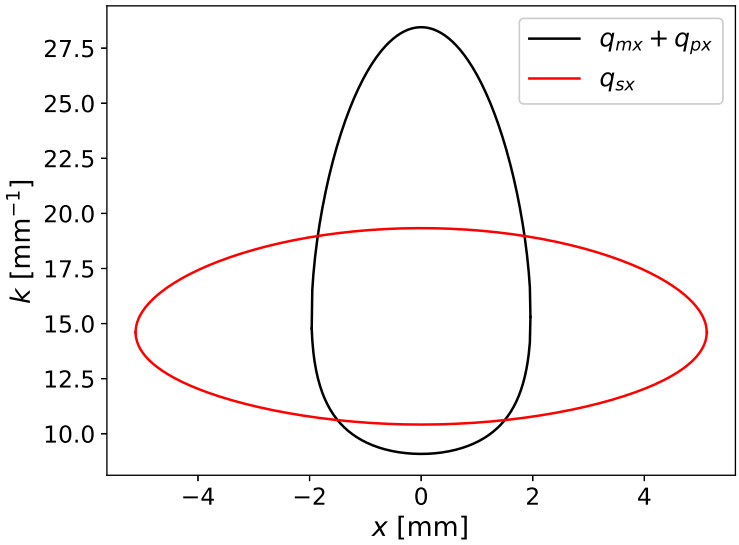

Figure 6. Dominant secondary decay for the primary daughter wave $\omega_m/(2\pi) = 70.0168$ GHz into the IBW $\omega_s/(2\pi) = 0.5615$ GHz and a downshifted UH wave.

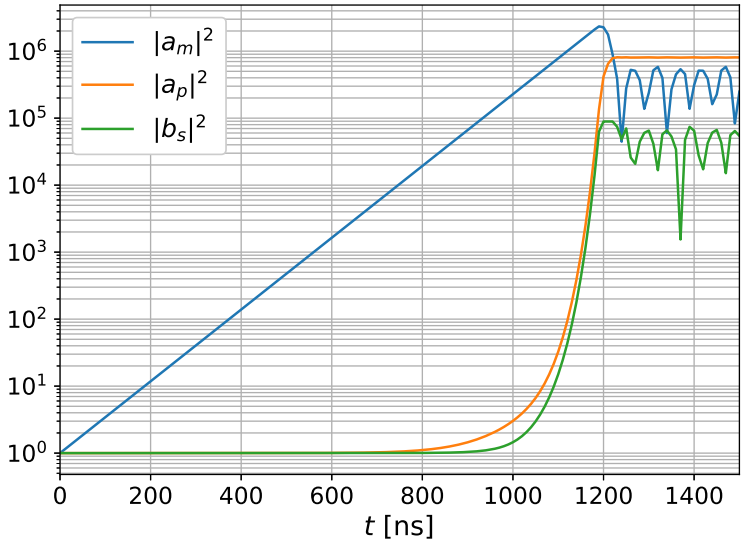

Figure 7. Evolution of the primary daughter mode a_m, as well as the secondary daughter modes a_p and b_s according to the system of equations in (15). The initial values correspond to the thermal levels and the pump intensity is $I_0 = 0.003$ kW/mm^2.

in timescales and levels. Both start with exponential growth of the primary daughter wave until about 800 ns after which a transition lasting about 350 ns takes place and the secondary UH daughter modes swiftly take over while draining the primary pump wave. From around 1150 ns, the system has reached a saturating phase as can be seen in figure 9 which shows the total energy of all the daughter modes.

Lastly, the absorption of the pump intensity is found by taking the time derivative of the total daughter mode energy density integrated over their trapping regions. This

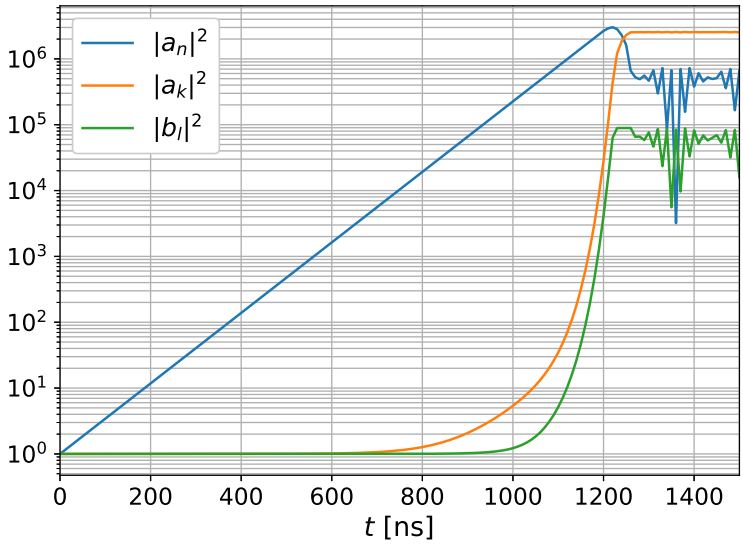

Figure 8. Evolution of the primary daughter mode a_n, as well as the secondary daughter modes a_k and b_l according to the system of equations in (15). The initial values correspond to the thermal levels and the pump intensity is $I_0 = 0.003$ kW/mm^2.

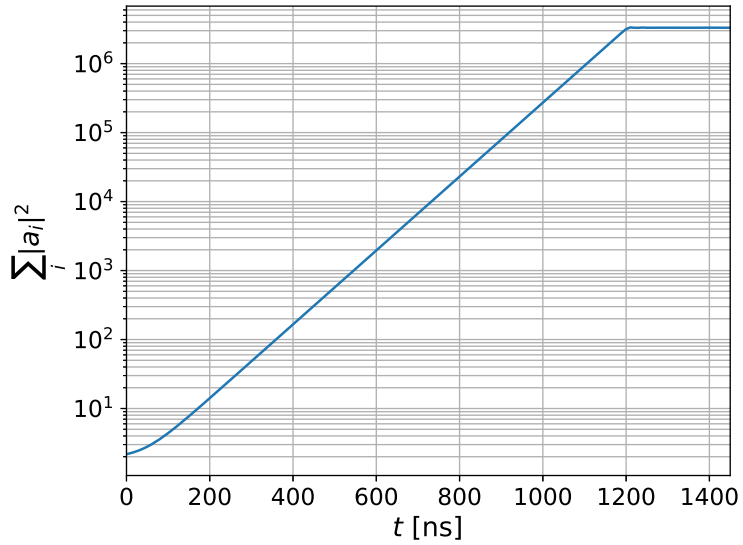

Figure 9. Evolution of the total energy contained in the primary and secondary daughter modes according to the system of equations in (15). The initial values correspond to the thermal levels and the pump intensity is $I_0 = 0.003$ kW/mm^2.

number is normalized to the input pump intensity and given the symbol α in figure 10. The absorption has an exponential growth phase for the first 1200 ns, peaking at about 3% for a pump intensity of $I_0 = 0.003$ kW/mm^2. After the saturating phase has set in, the absorption quickly decreases and fluctuating around zero.

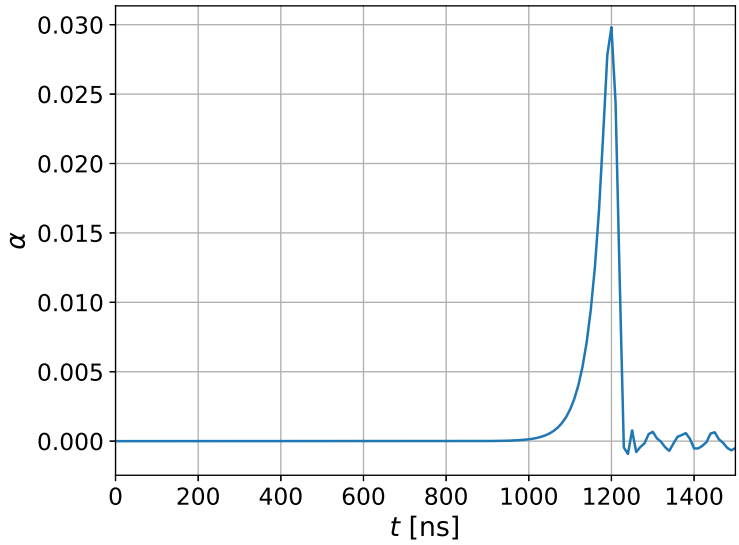

Figure 10. The absorption of the pump wave power per area as it propagates through the non-monotonic density structure and excites EBW and IBW daughter modes. The initial values for the daughter modes correspond to their thermal levels and the pump intensity is $I_0 = 0.003$ kW/mm^2.

3. Comparison with a fully kinetic code

3.1. Simulations

The PIC code EPOCH[42] is used for the fully kinetic simulations to be compared with the reduced model. For the PIC simulations, the parameters are the same with the exception of the density profile which has been modified slightly to reduce the size of the domain. The tails of the Gaussian profile are replaced with super-Gaussian ones on the form

$$n_e(x) = n_i(x) = \begin{cases} n_0 \exp(-[x/\ell]^2) & |x| \leq \ell \\ n_0 \exp(-[x/\ell]^4) & |x| \geq \ell \end{cases}. \tag{22}$$

This profile can be seen in figure 11. The lower frequency primary daughter mode, q_m, has the larger trapping region of the primary daughter waves. Its trapping region is unaffected by the change in the tails of the density profile. The simulation domain size is -1.6 cm $< x <$ 1.6 cm and there are $n_\mathrm{x} = 2660$ grid points in it such that the primary daughter waves have at least 20 grid points per wavelength. There are $n_\mathrm{part} = 10^4 n_\mathrm{x}$ super-particles of different weights to produce the desired density profile. To avoid discontinuities in the pump wave, the intensity is ramped up using $I = I_0 \frac{2}{\pi} \arctan(t/\tau_\mathrm{ramp})$. The values $I_0 = 0.003$ kW/mm^2 and $\tau_\mathrm{ramp} = 0.2$ ns are used for most figures in this section but a pump intensity scan is shown later. Open field boundary conditions are used while particles leaving the system are replaced by thermally distributed ones entering the system. The simulation ran for just over 10^3 ns with a time step of 0.95 times the longest allowed by the Courant-Friedrichs-Lewy stability condition[43].

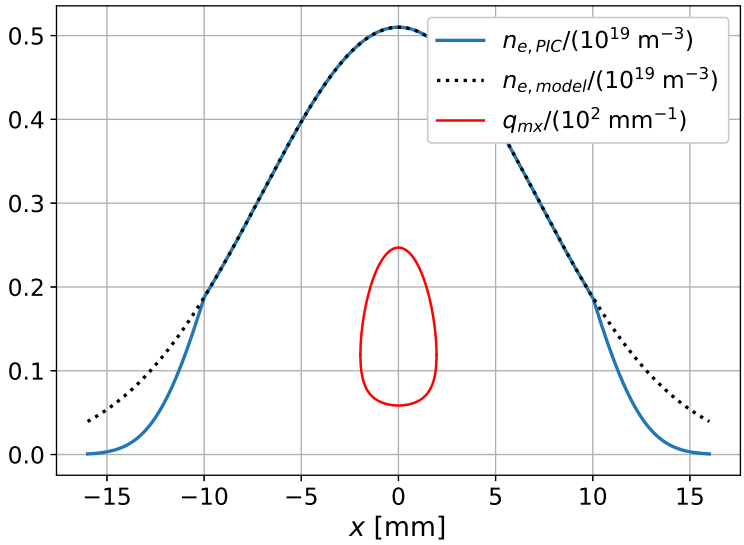

Figure 11. The density profile used in the PIC simulations (solid blue line) has super-Gaussian tails in order for them to fall off faster when $x > \ell$. The primary daughter waves are unaffected by the deviation between the profiles used for PIC and the reduced model (dotted black line), as the lower frequency daughter is trapped (solid red line) much closer to the density peak.

3.2. Primary decay

We apply an FFT to the longitudinal electric field in the center region of the domain, transforming both time and space. As can be seen in figure 12, the major peaks in the UH spectrum in the time window 900 ns $< t <$ 1040 ns agree well with the predicted primary daughter waves just below the UH frequency. Along the bottom white dotted line corresponding to ω_m, two major peaks are found at positive k. One is found along the X-mode dispersion curve and the other along the EBW dispersion curve. Both peaks are associated with the same trapped UH wave; the wave propagates in the negative x-direction as an EBW. As the density drops, the wave reaches the UH layer and is converted into an X-mode wave propagating in the positive direction, which is represented by the other peak. Similarly along the upper white dotted line, the two peaks at negative k represent the X-mode and EBW of the ω_n daughter waves.

3.3. Secondary daughters

In the main secondary decay processes, it was predicted in section 2 that each of the primary daughter waves decay into an IBW and a correspondingly downshifted UH wave. Moving a 140 ns FFT window in the later half of the simulation, the resulting time dependent UH spectrum is shown in figure 13. The predicted primary and secondary UH daughter wave frequencies are marked by horizontal dotted lines. Whilst the primary daughter wave frequencies are clearly in good agreement with the simulations, the dominant secondary UH daughter frequencies are less obvious. The spectrum is

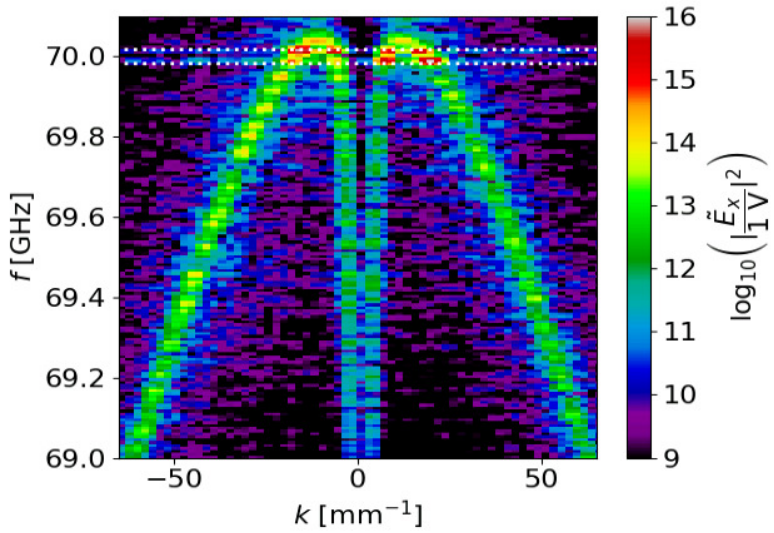

Figure 12. UH spectrum of the longitudinal electric field, E_x, for -0.15 cm $< x <$ 0.15 cm and 900 ns $< t <$ 1040 ns. The horizontal white dotted lines mark the primary daughter waves frequencies predicted in section 2.

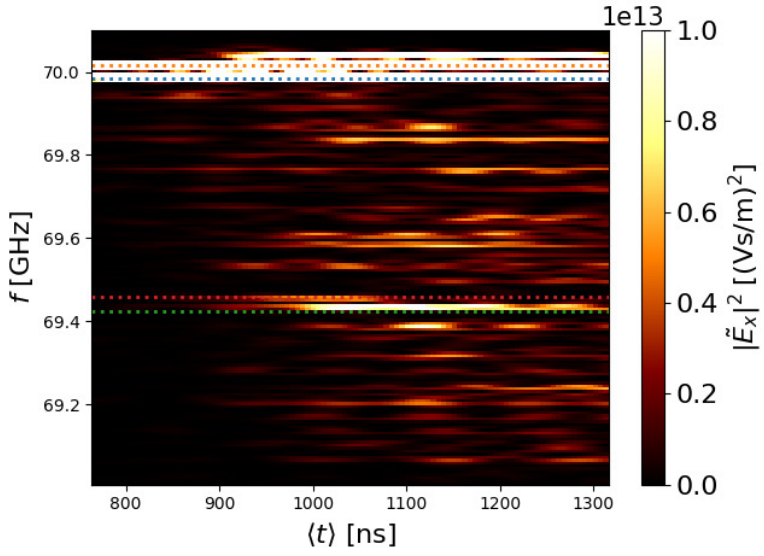

Figure 13. UH spectrum of the longitudinal electric field, E_x, at $x = 0$ mm as a function of time by moving a 140 ns FFT window in time. The $\langle t \rangle$ axis indicates the center of this FFT window. The horizontal dotted lines are the predicted primary (blue and orange) and secondary (red and green) UH daughter waves of greatest importance. Note that the level of the primary daughter waves far exceeds the shown range.

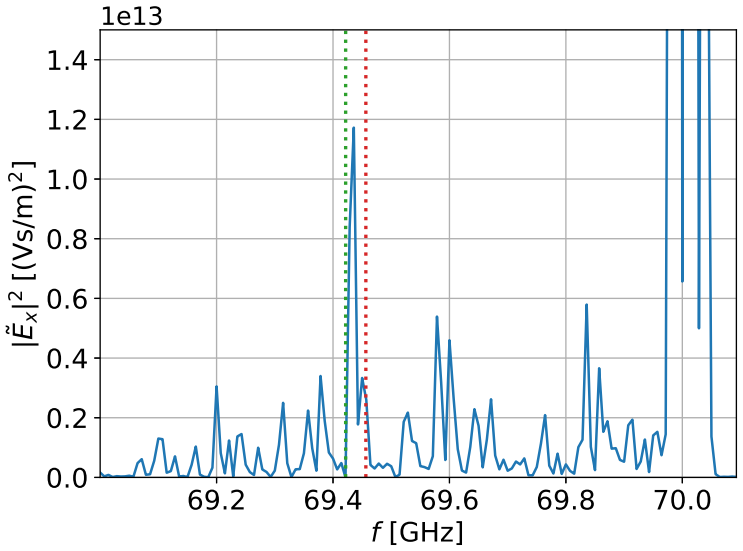

Figure 14. UH spectrum of the longitudinal electric field, E_x, for 1000 ns $< t <$ 1140 ns at $x = 0$ mm. The vertical dotted lines are the predicted secondary UH daughter waves of greatest importance. The green dotted line relates to ω_k and the red dotted line to ω_p.

fluctuating and some spectral lines are seen to be only momentarily visible. The earliest spectral line to appear is near 69.94 GHz, corresponding to around 0.05 GHz or 0.07 GHz downshifted from the primary daughter waves. With an ion cycltron frequency of $\omega_{ci}/(2\pi) = 0.04$ GHz, this would correspond to decay into the fundamental IBW branch. Still, lines corresponding to the predicted secondary UH daughter frequencies, which are marked by the red and green dotted lines, are also seen. The green dotted line corresponding to ω_k in particular is close to a strong spectral line. Figure 14 shows the levels in a line plot after a wide spectrum has been excited. Here, the line corresponding to the predicted secondary UH daughter wave at ω_k is seen to exceed the majority of spectrum, except of course for the primary daughter frequencies as well as a prominent upshifted peak around 70.04 GHz.

The corresponding secondary IBW daughter waves should be visible in the LH spectrum shown in figure 15. When comparing this figure with the UH spectrum in figure 13, the LH spectrum is even more intermittent. In spite of the intermittency, the spetrum is seen to be composed of individual spectral lines separated approximately by $\omega_{ci}/(2\pi) = 0.04$ GHz, which correspond to the IBW branches. The strongest of these lines are found near the LH frequency, $\omega_{\mathrm{LH}}/(2\pi) = 0.45$ GHz. Although there is some signal near the predicted secondary IBW daughter frequencies marked collectively by the horizontal line, they do not appear to be the dominant frequencies. It should be mentioned that the trapping regions of the IBWs are often larger than that of the UH waves, e.g. see figures 5 and 6. Whilst it may take a while for the IBW spectrum to reach $x = 0$ in figure 15, there really are no indications of the IBW levels predicted by the theoretical model anywhere in the domain. This suggests that the secondary

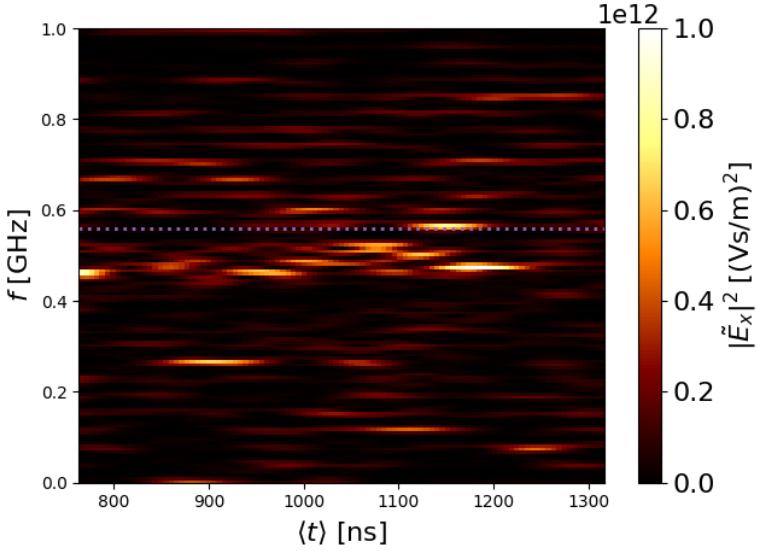

Figure 15. LH spectrum of the longitudinal electric field, E_x, at $x = 0$ mm as a function of time by moving a 140 ns FFT window in time. The $\langle t \rangle$ axis indicates the center of this FFT window. As the difference between the predicted secondary IBW daughter frequencies is very small when considering the frequency resolution, they are both represented by a single horizontal dotted line.

phase behaves differently than predicted by the analytical model. It is possible that the ion daughter waves are interacting more dynamically with each other, shifting energy between frequencies not considered in the limited cascade. For higher intensities, the ion temperature is found to increase by $\sim 10 - 15\%$ inside the cavity shortly after the primary instability saturates.

3.4. Growth

To estimate the growth rate of the primary decay process, we use two different methods. One is based on averaging the absolute squared longitudinal electric field inside the cavity as a measure of the population of UH plasmons. The other is based on integrating the spectral density near the primary daughter frequencies while changing the time window of the transformation. We run a series of simulations with varying pump intensity and use both methods to get an estimate of the growth rate as a function of pump intensity.

For the estimate using the first method, the quantity $|E_x|^2$ is averaged over -1.5 mm $< x <$ 1.5 mm, which is inside the trapping region of the primary daughter waves. As the primary daughter waves are excited through PDI, the field increases and the growth rate can be estimated by fitting an exponential to the growth phase. This is shown in figure 16 where several of the simulations appear to reach a saturation phase. The level at which the saturation sets in can be seen to depend on the pump intensity. Higher pump intensity results in a greater overshoot which then falls off. The growth rate as a function of pump wave intensity can be seen in figure 17 indicated by the blue circles.

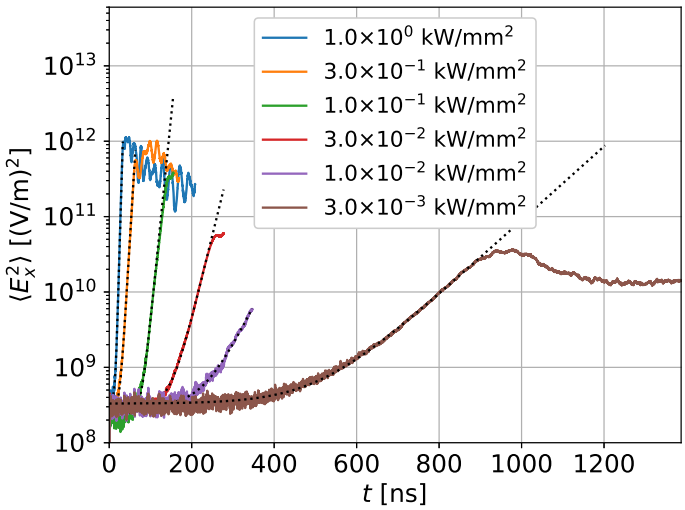

Figure 16. Squared longitudinal electric field averaged over -0.15 cm $< x <$ 0.15 cm as a function of time. Fitted exponential growth rates with constant offsets are plotted on top as black dotted lines.

The weakness of this method is that it is not possible to separate the contributions from different modes. This is not of much importance as long as it is the primary PDI that dominates.

For an estimate relying on the spectral power density, we transform E_x at $x = 0.0$ mm into frequency domain, using a moving time window of 30 ns to get an evolution of the spectrum. By integrating the range 69.9 GHz $< f <$ 70.1 GHz, we get an estimate of the population of primary daughter waves in the window of time. Fitting again an exponential to the primary growth phase, the orange stars in figure 17 are obtained. The estimated growth rates agree well with those obtained by averaging the electric field, except at the highest pump intensity, where the growth estimate from this method unexpectedly drops off. This is likely because saturation is reached on a time scale similar to the FFT time window and a good estimate therefore cannot be made with this method. The two methods generally agree well with the exception of the highest intensity point where the FFT method is unreliable while the mean field method continues the trend well. The prediction based on the reduced model generally agrees well with the results from the PIC simulation, staying within a factor of 2 for all points. The agreement is better in the weakly nonlinear regime than in the strongly nonlinear regime. Since an absolute instability clearly takes place for $Z < 1$, a convective PDI cannot explain these results. The theory of low threshold absolute PDI does not apply in the strongly nonlinear regime where $Z \gg 1$, but the high intensity simulations are included to investigate how the PIC results scale with intensity and the deviation from the reduced model. It is seen that the reduced model predicts a $\gamma \propto I_0^{1/2}$ trend whereas the PIC simulations indicate a steeper trend. The low intensity points are close to $\gamma \propto I_0^{3/4}$ but the trend changes slightly and is closer to $\gamma \propto I_0^{2/3}$ at higher intensities. It can be seen that the FFT method predicts a weaker relation between

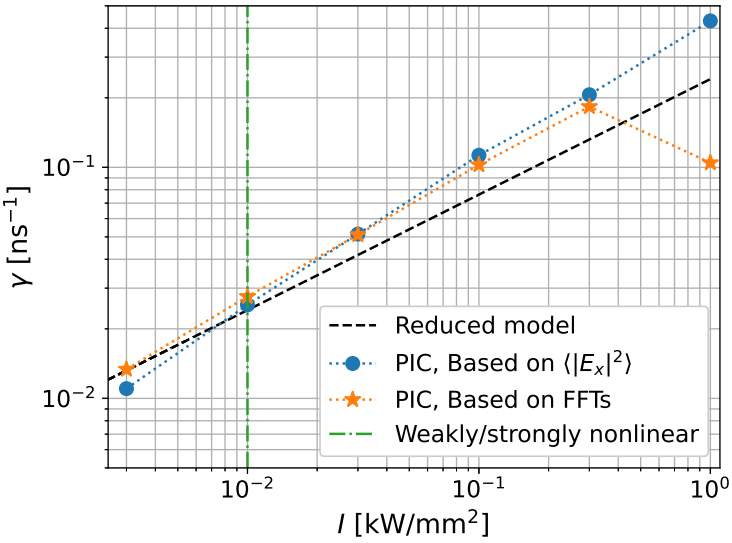

Figure 17. Primary PDI growth rates as functions of the pump wave intensity. The markers represent two different methods applied to the PIC simulations. The dashed black line shows the primary growth rate based on the reduced model. The dashed-dotted green vertical line marks the transition between the weakly and strongly nonlinear regimes, i.e. at $Z = 1$.

γ and I_0 which is perhaps because it is better at limiting the number of contributing frequencies and processes. At higher pump intensities especially, there are indications that the large amplitude fields from the eigenmodes give rise to quasistationary electron and ion density perturbations. These perturbations do not oscillate and can exist for ~ 100 ns with only minor changes, which means that they can modify the background densities from the point of view of the excited modes. Such effects likely affect the eigenfrequencies and the nonlinear coupling of modes, but they are not included in the analytical model presented in section 2. The impact of these quasistationary density perturbations will be the subject of future investigations.

Using the FFT method, the temporal evolution of the predicted primary and secondary daughter wave populations for $I_0 = 0.003$ kW/mm^2 are shown in figure 18. Higher spectral resolution is necessary to separate the modes so the FFT time windows are increased to 139 ns which comes at a cost of temporal resolution. As can be seen in figure 18, the primary daughter wave ω_m grows exponentially from the beginning of the simulation whereas ω_n first appears somewhat constant but is compensated by a jump at around 200 ns and displays similar behavior as ω_m thereafter. They both peak after around 1000 ns at an amplitude of more than 10^4 times their initial level. They then fall off and appear to saturate around 10^4. The secondary daughter wave ω_p appears to fluctuate around its initial population for approximately 600 ns after which it too starts growing exponentially at a similar rate. It peaks at an amplification of around 10^3 after 1100 ns and then appears to fall off. The other secondary UH daughter wave, ω_k, starts growing exponentially at around 700 ns but is also compensated by an initial jump,

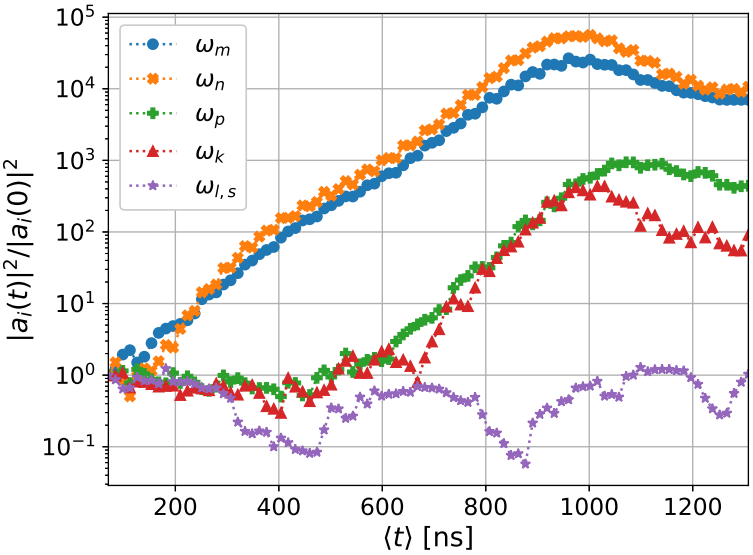

Figure 18. Primary and secondary UH daughter populations normalized to their initial values. Points are generated by FFTs of E_x in time windows of 139 ns and integrating the spectral density around the relevant frequencies. This method does not differentiate modes of the same frequency but with opposite sign of k.

after which it follows ω_p closely until the 1000 ns mark after which it falls off quicker than ω_k. The combined contributions from the IBWs in $\omega_{l,s}$ do not display any signs of growth. Rather, the signal appears to be somewhat periodic with a period of around 500 ns. There are weak indications of more activity at the end of the simulation.

When comparing the $I_0 = 0.003$ kW/mm^2 line in figure 16 as well as the primary modes in figure 18 from the PIC simulations with what is predicted by the reduced model in figure 9, saturation appears to be reached quicker at around 950 ns in the PIC simulations but around 1150 ns in the reduced model. Better agreement could be reached by adding more subsequent decays to the system of equations in (15) in order to decrease the saturation time.

3.5. Absorption

By transforming the transverse electric field at the boundaries and integrating the spectral density over the range 139.9 GHz $< \omega/(2\pi) <$ 140.1 GHz, we can compare the intensity of the pump wave entering and leaving the domain. By subtracting the ratio of the intensities from unity, we get a measure of the absorption, α, in non-monotonic density structure, which is shown in figure 19. The absorption is seen to grow up to about 4.5% of the pump wave intensity at around 900 ns after which the absorption starts to oscillate strongly, suggesting a secondary phase is setting in, which is in agreement with figure 16. Unlike the numerical integration of the reduced model in figure 10, the results from the PIC simulations in figure 19 show a more dynamical saturation phase which stays in the vicinity of 1%. Again, the saturation phase of the reduced model may also become more dynamical by adding more daughter modes to the

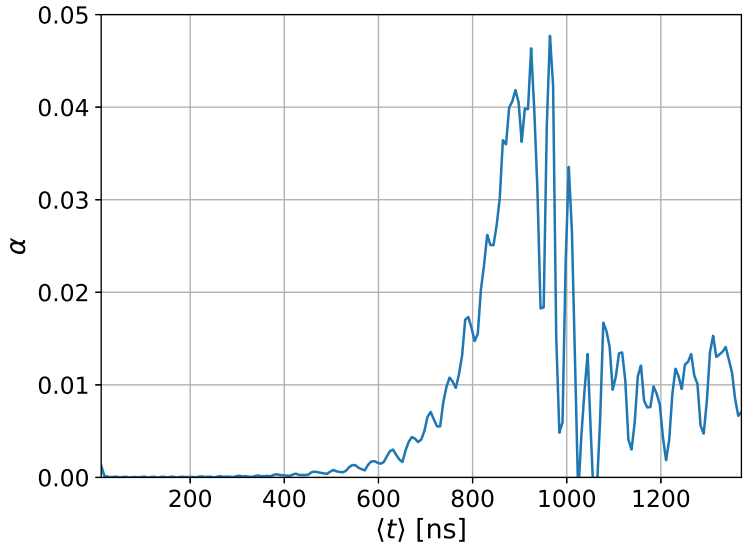

Figure 19. Absorption of the pump wave power per area, obtained by comparing the transverse electric field intensity near the pump wave frequency at the ends of the domain.

decay cascade. Perhaps the absorption predicted to peak at 3% could then get closer to the 4.5% in the PIC simulations.

4. Discussion and conclusion

A reduced 1D model describing an absolute PDI of a high power microwave beam feeding a cascade of decays into UH waves and IBWs trapped in a non-monotonic density profile was compared to 1D fully kinetic PIC simulations. The cascade in the analytical model featured a single primary decay of a fast X-mode wave into two UH eigenmodes followed by two secondary decays producing an UH and an IBW eigenmode from each of the primary daughter modes. The analytical model produced a system of coupled differential equations which were solved numerically. The PIC simulations made no assumptions about the nonlinear wave interactions. The two models showed good agreement regarding the primary decay frequencies, growth rate and saturation timescale, in particular in the weakly nonlinear regime. The secondary UH daughter eigenmodes of the reduced model are clearly visible in the spectra of the PIC simulations, however, so are several other frequencies. Some of these other frequencies precede the predicted secondary UH waves while other exceed them. The reduced model predicts two secondary IBW daughter modes with frequencies exceeding the local LH frequency slightly. This is not observed clearly in the PIC spectra. Better agreement with the PIC simulations might be obtained by adding more decays to the reduced analytical model or by decreasing the pump intensity of the pump wave further. This would slow the transition into the saturation phase down. It is also possible that the reduced model must be expanded to include additional physical mechanisms, such as a modification

to the background density produced by the eigenmodes, in order to properly model the secondary decays.
Numerical integration of the reduced analytical model provides a significantly cheaper alternative to fully kinetic simulation and they have shown good agreement in the right pump intensity regime. The reduced model describes the primary instability well which is needed to estimate a threshold for the absolute PDI as well as its impact.

5. Acknowledgments

This work has been supported by research grant 15483 from VILLUM FONDEN and the Enabling Reseach grant ENR-MFE19.DTU-03 from the EUROfusion Consortium. The work has been carried out within the framework of the EUROfusion Consortium and has received funding from the Euratom research and training programme 2014-2018 and 2019-2020 under grant agreement No 633053. The views and opinions expressed herein do not necessarily reflect those of the European Commission. Furthermore, the PDI theory presentation in the second section is supported under the Ioffe Institute state contract 0040-2019-0023, whereas the numerical modelling interpretation presented in the same section is supported under the Ioffe Institute state contract 0034-2021-0003. The EPOCH code used in this work was in part funded by the UK EPSRC grants EP/G054950/1, EP/G056803/1, EP/G055165/1, EP/ M022463/1 and EP/P02212X/1.

References

[1] Silin, V. P., 1965, Sov. Phys. JETP, **20**, 1510
[2] Aliev, Yu. M., Silin,V. P., Watson, C., 1966, Sov. Phys. JETP, **23**, 626
[3] Gorbunov, L. M., Silin, V. P., 1966, Sov. Phys. JETP, **22**, 1347
[4] Jackson, E. A., 1967, Phys. Rev., **153**, 255.
[5] Silin, V. P., 1967, Sov. Phys. JETP, **24**, 1242.
[6] Bers, A., and Reiman, A., 1975, Proceedings of the 7th Conference on Numerical Simulation of Plasmas, Courant Institute, N. Y.U., June 1975, p. 192.
[7] Bers, A., Kaup, D. J., and Reiman, A., 1976, Phys. Rev. Lett., **37**, 182.
[8] Kaup, D. J., Reiman, A., Bers, A., 1979, Reviews of Modern Physics, **51**, 275.
[9] Piliya, A. D., 1971, Proceedings of 10th Conf. Phenomena in Ionized Gases (Oxford), 320
[10] Rosenbluth, M. N., 1972, Phys. Rev. Lett., **29**, 565.
[11] Piliya, A. D., 1973, Sov. Phys. JETP, **37**, 629.
[12] Piliya, A. D., 1973, JETP Letters, **17**, 266.
[13] Rosenbluth, M. N., White, R. B., and Liu, C. S., 1973, Phys. Rev. Lett., **31**, 1190.
[14] Popov A. Yu. and Gusakov E. Z., 2015, Plasma Phys. Control. Fusion, **57**, 025022
[15] Hansen S. K. *et al*, 2021, *Plasma Phys. Control. Fusion*, **63**, 095002
[16] Bornatici M. *et al*, 1983, Nuclear Fusion, **23**, 1153
[17] Stober J. *et al*, Plasma Phys. Control. Fusion **62** (2020) 024012
[18] McDermott F. S. *et al*, 1982, The Physics of Fluids **25** 1488
[19] White R. B., Chen F. F., 1974, Plasma Physics, **16**, 565
[20] Laqua H. P. *et al*, 1997, Physical Review Letters, **78**, 18
[21] Hansen S. K. *et al*, 2017, Plasma Phys. Control. Fusion, **59**, 105006
[22] Bulyginsky D. G. *et al*, 1984, Proc. 11th European Conf. Controlled Fusion and Plasma Physics, vol 1, 457

[23] Wilhelm R. *et al*, 1984, Plasma Phys. Control. Fusion, **26**, 1433
[24] Pietrzyk Z. A. *et al*, 1993, Nucl. Fusion, **33**, 197
[25] Westerhof E. et al., 2009, Phys. Rev. Lett., **103**, 125001
[26] Nielsen S.K., Salewski M., Westerhof E. et al., 2013, Plasma Phys. Control. Fusion, **55**, 115003
[27] Gusakov E. Z. and Popov A. Yu., 2010, Phys. Rev. Lett., **105**, 115003
[28] Gusakov E. Z. and Popov A. Yu., 2016, Physics of Plasmas, 23, 082503
[29] Tancetti A., Nielsen S. K., Rasmussen J., Gusakov E. Z., Popov A. Yu., Moseev D., Stange T., Senstius M. G., Killer C., Vecséi M., Jensen T., Zanini M., Abramovic I., Stejner M., Anda G., Dunai D., Zoletnik S., Laqua H. P. and the W7-X Team, 2022, Nucl. Fusion **62** 074003
[30] Altukhov A. B. *et al*, 2019, EPL, **126**, 15002
[31] Gusakov E. Z., Popov A. Yu., and Saveliev A. N., 2019, Plasma Phys. Control. Fusion, **61**, 025006
[32] Gusakov E. Z. and Popov A. Yu., 2020, Phys. Usp., **63**, 365
[33] Senstius M. G., Nielsen S.K., Vann R. G. L., 2020, Phys. Plasmas, 27, 062102
[34] Senstius M. G. *et al*, 2021, Plasma Phys. Control. Fusion, **63**, 065018
[35] Reiman, A., 1979, Reviews of Modern Physics, **51**, 331.
[36] Gusakov, E. Z., Fedorov, V. I., 1979, Sov. J. Plasma Phys., **5**, 263
[37] Gusakov, E. Z., Fedorov, V. I., 1979, Sov. J. Plasma Phys., **5**, 463
[38] Akhiezer A. I. and Akhiezer I. A., 1975, *Plasma Electrodynamics: Linear Theory* (Oxford: Pergamon)
[39] Berk, H. L. and Book, D. L., 1969, The Physics of Fluids **12**, 649
[40] Hansen, S. K., 2019, Parametric decay instabilities in the electron cyclotron resonance heating beams at ASDEX upgrade, PhD thesis, DTU
[41] Karney C. F. F. and Bers A., 1977, Phys. Rev. Lett., **39**, 550
[42] Arber T. D. *et al*, Plasma Phys. Control. Fusion **57** (2015) 113001
[43] Taflove A. and Hagness S. C. 2000 *Computational Electrodynamics: The Finite-Difference Time-Domain Method* 2nd edition (Norwood, MA: Artech House)